arTs Università degli Studi di Trieste
Archivio della ricerca – postprint

Modeling and Analysis of Synchronous Reluctance Machines With Circular Flux Barriers Through Conformal Mapping

Alberto Tessarolo

Department of Engineering and Architecture, University of Trieste, Trieste 34127, Italy

Synchronous reluctance (SynRel) machines are gaining more and more importance in various fields of application thanks to their known merits like rugged construction, high efficiency, absence of field windings, and no or reduced need for permanent magnets. Out of the possible design variants, in this paper, SynRel motors with uniform mechanical air gap and circularly shaped flux barriers are considered and a conformal-mapping approach to their analytical modeling and simulation is proposed. A suitable conformal transformation is introduced to compute the reluctance of each rotor circularly shaped flux barrier and the result is then used to analytically determine the air-gap flux density distribution and the electromagnetic torque of the machine in arbitrary operating conditions. The accuracy of the methodology proposed is assessed against finite element analysis.

***Index Terms*— Analytical methods, conformal mapping, flux barriers, synchronous reluctance (SynRel) machines.**

I. Introduction

SINCE they were first proposed, in the 1920s [1], synchronous reluctance (SynRel) motors have found little applications for many years due to their poor efficiency and power factor when supplied from the grid. During the 1990s, with the advent of modern variable-frequency converters and digital control systems, these motors disclosed their potentialities as possible competitive alternatives to traditional induction motor drives [2], [3]. Furthermore, optimized rotor designs were proposed to achieve better power factor values [4]. In recent years, a large amount of work has been carried out to optimize SynRel motor performance in terms of torque pulsations [5]–[8], copper losses [9], core losses [10], [11], and overall efficiency [12]. Presently, SynRel motors appear strongly attractive in many fields, like vehicle traction [13], [14] and household appliances [15], [16], due to the widely recognized benefits they bring in terms of [17]: rugged construction, high-speed capabilities, absence of excitation winding, and removed or strongly reduced need for permanent magnets. Improvements in the machine torque density can be, in fact, obtained with limited use of rare-earth permanent magnets or low-cost ferrite ones, in the so-called permanent-magnet-assisted SynRel (PMaSynRel) configurations [17]–[20].

SynRel motor principle of operation lies on the different reluctance (magnetic anisotropy) that the rotor exhibits along orthogonal d and q axes [1], [2]. Such anisotropy can be obtained in different ways, such as by suitably shaping rotor outer profile [1], [4]; however, the most widespread SynRel design includes a round rotor with uniform mechanical air gap and appropriately designed flux barriers [21], [22].

Rotor flux barriers can be shaped according to different possible geometries [21]. The most typical ones, shown in Fig. 1, are the so-called C-shape [Fig. 1(a)] and the circular (or round) shape [Fig. 1(b)]. The former case, wherein the barrier is composed of one or more straight segments, is particularly suitable for PMaSynRel motors as it allows for simple accommodation of parallelepiped-shaped permanent magnets inside the barrier [6], [9], [10], [17]–[20]; round barriers, instead, are preferably employed in permanent-magnet-free SynRel machines [4], [12], [13], [16], [21].

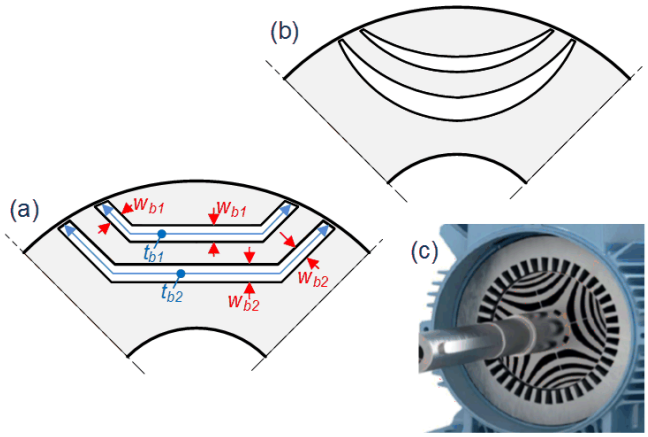

Fig. 1. (a) SynRel rotor with C-shaped barriers. (b) SynRel rotor with circular barriers. (c) Example of SynRel motor with circular barriers.

One of the challenges in the analysis of SynRel motors is the fast but accurate prediction of their performance from design data. Analytical methods, based on magnetic equivalent circuit (MEC) methods, have been proposed for this purpose [6], [7], [10], [11]. These approaches have been applied to both SynRel and PMaSynRel motors with C-shaped barriers and assume that each barrier has a uniform width [w_b in Fig. 1(a)]. Under such hypothesis, it is possible to elementarily compute the reluctance of a flux barrier based on its two characteristic dimensions indicated as w_b and t_b in Fig. 1(a). The method, however, may be hardly extended to the case of circular barriers [Fig. 1(b)] which can have a significantly nonuniform width like in the commercial construction example shown in Fig. 1(c) [23].

In this paper, SynRel machines with circular flux barriers are considered and a method is presented to compute the

Corresponding author: A. Tessarolo (e-mail: atessarolo@ units.it).

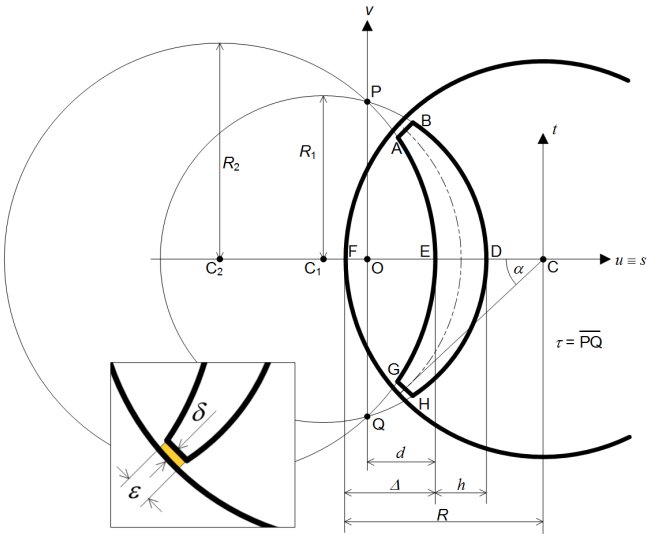

Fig. 2. Geometry assumed for a single circular flux barrier and relevant characteristic dimensions.

reluctance of each circularly shaped barrier through conformal mapping [24]. Based on this calculation, it is shown how the air-gap flux density and the electromagnetic torque of the machine can be analytically determined through a MEC approach. The accuracy of the methodology proposed is assessed by comparison against finite element analysis (FEA) simulations on a sample SynRel motor where magnetic saturation effects are considered.

This paper is organized as follows. In Section II, the geometric model assumed for a circular-barrier SynRel motor is analyzed. In Section III, a suitable conformal map is introduced to study the magnetic field in each circular flux barrier. In Section IV, the reluctance and stored magnetic energy of a circular flux barrier are computed by the proposed conformal map. In Section V, the presented theory is applied to analytically compute the air-gap flux density and the electromagnetic torque of an example SynRel motor and results are assessed by comparison against FEA simulations.

II. Geometric Model Description

In the following of this paper, SynRel motors are considered featuring a rotor topology with one or more circular flux barriers, each assumed to have the shape shown in Fig. 2.

According to this modeling, the machine rotor (of axial length L) has center C and radius R; barrier contours AG and BH are assumed to be circumferential arcs, respectively, belonging to circles of centers C_2 and C_1 and radii R_2 and R_1, while contours AB and GH are approximated as straight segments. Hence, each flux barrier profile is fully determined by the five independent design parameters Δ, h, δ, ε, and α (Fig. 2), where α is the angle between the horizontal line passing through C and the line connecting C with the central point of segment GH.

Under the above hypotheses and introducing a Cartesian reference frame of axes s and t centered in C (Fig. 2), we can identify any generic point M of the plane with its coordinate pair (s_M, t_M). For points A, B, D, and E, we have

$$\begin{aligned} s_A &= (R-\delta)\cos\left(\pi-\alpha+\frac{\varepsilon}{2R}\right), \\ t_A &= (R-\delta)\sin\left(\pi-\alpha+\frac{\varepsilon}{2R}\right) \end{aligned} \tag{1}$$

$$\begin{aligned} s_B &= (R-\delta)\cos\left(\pi-\alpha-\frac{\varepsilon}{2R}\right), \\ t_B &= (R-\delta)\sin\left(\pi-\alpha-\frac{\varepsilon}{2R}\right) \end{aligned} \tag{2}$$

$$s_D = -R+\Delta+h, \quad t_D = 0, \quad s_E = -R+\Delta, \quad t_E = 0 \tag{3}$$

where (1) and (2) hold under the hypothesis that $\varepsilon \ll R$ as it normally occurs in SynRel motor design.

From the geometric considerations explained in Appendix, we can determine the s coordinate of circle centers C_1 and C_2 as

$$s_{C_1} = \frac{s_B^2 + t_B^2 - (\Delta - R + h)^2}{2(R - \Delta - h + s_B)}, \quad s_{C_2} = \frac{s_A^2 + t_A^2 - (R-\Delta)^2}{2(R - \Delta + s_A)} \tag{4}$$

and the corresponding circle radii R_1 and R_2 as

$$R_1 = -R + \Delta + h - s_{C_1}, \quad R_2 = -R + \Delta - s_{C_2}. \tag{5}$$

The intersection point P between the two circles of radii R_1 and R_2 and centers C_1 and C_2 has coordinates

$$s_P = \frac{R_1^2 - R_2^2 - s_{C_1}^2 + s_{C_2}^2}{2(s_{C_2} - s_{C_1})}, \quad t_P = \sqrt{R_1^2 - (s_P - s_{C_1})^2}. \tag{6}$$

Thus, we can define the two lengths $d = \overline{OE}$ and $\tau = \overline{PQ}$ (Fig. 2) as

$$d = \overline{OE} = -R + \Delta - s_P, \quad \tau = \overline{PQ} = 2\,t_P. \tag{7}$$

Calling O the intersection of the s axis with segment PQ, we can fix a new reference frame centered at point O and having axes u and v, as shown in Fig. 2. This new reference frame identifies a complex plane $w = u + jv$ (being j the imaginary unit) that will be used in the next section for the conformal mapping of the flux barrier geometry. In particular, for the following it is worth observing that points A and G in the u and v reference frame have coordinates:

$$u_A = u_G = s_A + \overline{OC} = s_A + R - \Delta + d, \quad v_A = -v_G = t_A. \tag{8}$$

III. Conformal Mapping of the Flux Barrier Geometry

The physical complex plane $w = u + jv$ identified by the origin O and axes u and v (Fig. 2) can be mapped into a new complex plane $z = x + jy$ (Fig. 3) through the conformal transformation

$$z = f(w) = \mathrm{Arctan}(2w/\tau) \tag{9}$$

whose inverse is

$$w = f^{-1}(z) = g(z) = (\tau/2)\tan(z) \tag{10}$$

where Arctan() indicates the principal value of the complex inverse tangent function [25].

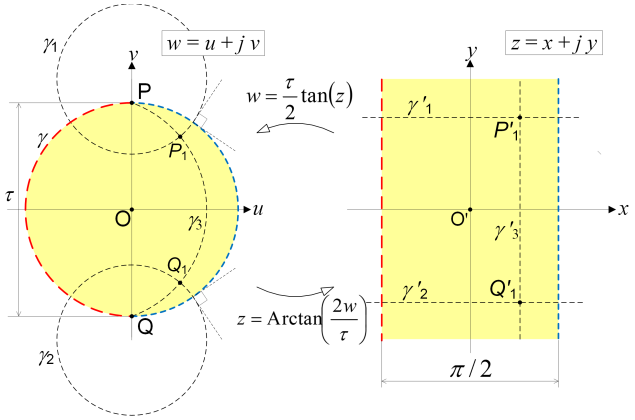

Fig. 3. Conformal transformation mapping circles of the w plane into straight lines of the z plane.

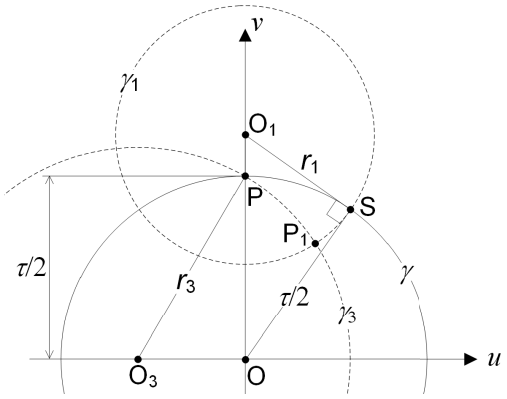

Fig. 4. Circumferences γ, γ_1, and γ_3 with their centers (O, O_1, and O_3, respectively), radii ($\tau/2$, r_1, and r_3, respectively), and intersection points (P, P_1, and S, respectively).

A. Analytical Properties of the Chosen Map

The complex map (9) can be equivalently written as [25]

$$z = x + jy = f(w) = \frac{j}{2}\mathrm{Ln}\left(\frac{\tau - 2jw}{\tau + 2jw}\right) = -\frac{1}{2}\mathrm{Arg}\left(\frac{\tau - 2jw}{\tau + 2jw}\right) + \frac{j}{2}\ln\left|\frac{\tau - 2jw}{\tau + 2jw}\right| \tag{11}$$

where Ln() is the principal value of the complex logarithm and $\mathrm{Arg}(Z) = \mathrm{atan2}(\mathrm{Re}(Z), \mathrm{Im}(Z))$ returns the argument of Z as a number between $-\pi$ and π.

In terms of the real and imaginary parts (u, v) of w, the complex function (11) naturally leads to define the real functions

$$x(u,v) = -\frac{1}{2}\mathrm{Arg}\left[\frac{\tau - 2j(u+jv)}{\tau + 2j(u+jv)}\right],$$
$$y(u,v) = \frac{1}{2}\ln\left|\frac{\tau - 2j(u+jv)}{\tau + 2j(u+jv)}\right| \tag{12}$$

which, through elementary passages, can rewritten as

$$x(u,v) = \frac{1}{2}\mathrm{atan}\left[\frac{\tau\, u}{(\tau/2)^2 - (u^2+v^2)}\right] \tag{13}$$

$$y(u,v) = \frac{1}{4}\ln\left[\frac{(\tau/2+v)^2 + u^2}{(\tau/2-v)^2 + u^2}\right]. \tag{14}$$

B. Geometric Properties of the Chosen Map

From a geometric point of view, the chosen map (9) transforms circles of the w plane into straight lines of the z plane, as shown in Fig. 3. The geometric properties of the map are explained below by applying it to circular curves of the w plane like γ_1–γ_3 (Fig. 3).

1) Circular Arcs (Like γ_3) Connecting Points P and Q: An example of a circumference passing through points P and Q is indicated as γ_3 in Figs. 3 and 4. Calling r_3 its radius and O_3 its center, from Fig. 4 it clearly results that the Cartesian equation of γ_3 is

$$\left(u \pm \sqrt{r_3^2 - (\tau/2)^2}\right)^2 + v^2 = r_3^2 \tag{15}$$

where the sign $+$ or $-$ applies depending on whether the arc is in the $u > 0$ or $u < 0$ half-plane, respectively. The condition $r_3 \geq \tau/2$ must be naturally satisfied. Substitution of (15) into (13) gives, after elementary passages

$$x = \pm\frac{1}{2}\mathrm{atan}\left[\frac{\tau/2}{\sqrt{r_3^2 - (\tau/2)^2}}\right] \tag{16}$$

where it is clear that $-\pi/4 < x < \pi/4$. Equation (16), in particular, gives

$$\lim_{r_3 \to \tau/2} x = \pm\frac{\pi}{4}. \tag{17}$$

We can therefore state that each circular arc (like γ_3) connecting P and Q in the w plane is mapped into a vertical line (like γ_3') of the z plane included in the strip $-\pi/4 < x < \pi/4$. In particular, the circumference γ of center O and radius $\tau/2$ is mapped into the borders of such strip.

2) Circumferences (Like γ_1 and γ_2) With Center on the v Axis and Orthogonally Intersecting γ: Examples of such circumferences are indicated as γ_1 and γ_2 in Figs. 3 and 4. Taking γ_1 for instance and calling r_1 its radius and O_1 its center, Fig. 4 shows how triangle O_1SO is a right-angled one, hence γ_1 Cartesian equation is

$$u^2 + \left(v \pm \sqrt{r_1^2 + (\tau/2)^2}\right)^2 = r_1^2 \tag{18}$$

with sign $+$ or $-$ to be chosen depending on whether O_1 is placed in the $v < 0$ or $v > 0$ half-plane, respectively. If we substitute (18) into (14), we find

$$y = \mp\frac{1}{2}\ln\left(\frac{\sqrt{\tau^2 + 4r_1^2} + \tau}{\sqrt{\tau^2 + 4r_1^2} - \tau}\right). \tag{19}$$

Therefore, circumferences (like γ_1) having their center on the v axis and orthogonally intersecting γ in the w plane are mapped into horizontal straight lines (like γ_1') of the z plane.

For the following, it is worth noting that if a circumference (like γ_1) orthogonally intersects γ, this implies that it also orthogonally intersects any circumference (like γ_3) passing through points P and Q. To prove this, we need to demonstrate

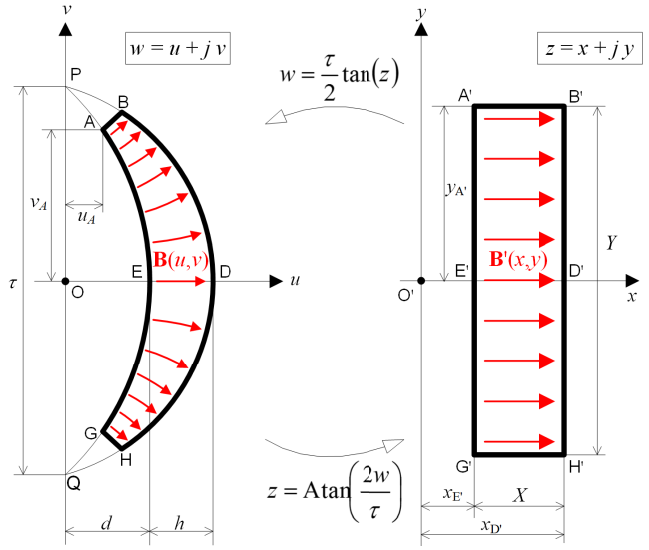

Fig. 5. Transformation of the flux barrier geometry (w plane) into a rectangle (z plane) through conformal map $z = f(w)$.

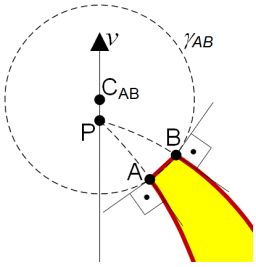

Fig. 6. Segment AB at flux barrier end and circumference γ_{AB} that orthogonally intersects flux barrier circular borders at points A and B.

that $O_1P_1O_3$ (Fig. 4) is a right-angled triangle. Elementary considerations lead to write

$$\overline{OO_1} = \sqrt{r_1^2 + (\tau/2)^2}, \quad \overline{OO_3} = \sqrt{r_3^2 - (\tau/2)^2}$$
$$\Rightarrow \overline{O_1O_3} = \sqrt{\overline{OO_1}^2 + \overline{OO_3}^2} = \sqrt{r_1^2 + r_3^2} \qquad (20)$$

and since $\overline{O_1P_1} = r_1$ and $\overline{O_3P_1} = r_3$, Pitagora theorem is easily seen to hold for triangle $O_1P_1O_3$.

C. Map Application to Flux Barrier Geometry

The conformal map $z = f(w)$ given by (11) naturally applies to the geometry of a flux barrier (Fig. 2, w plane) transforming it into a rectangle (z plane), as shown in Fig. 5. Actually, the proposed mapping involves a certain degree of approximation. According to the geometric property of the map $z = f(w)$ discussed in Section III-B, the flux barrier image in the z plane would be an exact rectangle only if the barrier side AB (Fig. 2) were modeled as a circular arc lying on the circumference γ_{AB} which orthogonally intersects the barrier in points A and B, as shown in Fig. 6. Nevertheless, given the very small size of AB, it can reasonably understood (and will be later assessed by comparison against FEA) that its approximation through a straight segment or through an arc of circumference γ_{AB} leads to practically overlapping results.

The dimensions X and Y of the rectangle in the z plane as well as its distance x_1 from the y-axis can be found considering that points D' and E' are the images of D and E through the map (9). This leads to write the equalities (Fig. 5)

$$x_{E'} = \mathrm{Arctan}(2u_E/\tau) = \arctan(2d/\tau) \qquad (21)$$
$$x_{D'} = \mathrm{Arctan}(2u_D/\tau) = \arctan[2(d+h)/\tau]. \qquad (22)$$

The rectangle width X is then determined as

$$X = x_{D'} - x_{E'}. \qquad (23)$$

As regards rectangle height Y, we can observe that the coordinate $y_{A'}$ of point A' (image of A) results from (14) as

$$y_{A'} = \frac{1}{4}\ln\left[\frac{(\tau/2 + v_A)^2 + u_A^2}{(\tau/2 - v_A)^2 + u_A^2}\right] \qquad (24)$$

where coordinates u_A and v_A of point A are given by (8). The rectangle height Y will be then (Fig. 5)

$$Y = 2y_{A'}. \qquad (25)$$

IV. Barrier Reluctance and Magnetic Energy Computation

In this section, the introduced conformal map is used to compute the magnetic reluctance of a flux barrier as well as an expression for the magnetic energy stored in it. This will be done in various steps as discussed below.

A. Field Determination in the Flux Barrier

As a first step, we need to fix boundary conditions so that the field inside the barrier can be determined. Along barrier borders AG and BH it is reasonable to suppose that Neumann boundary conditions hold, provided that the permeability of the core can be supposed infinitely high except for the iron bridge region, where some magnetic saturation inevitably occurs. On segments AB and GH, Neumann boundary conditions do not hold because, due to saturation, the permeability of the iron bridge is supposed to be relatively low. The approximation is hereinafter chosen of imposing a Dirichlet boundary conditions on segments AB and GH, which is equivalent to assuming that no flux lines cross these segments. Such an assumption sounds reasonable since segments AB are, by design, extremely small compared the overall barrier dimensions (as a case limit, they could be imagined to collapse into a single point), hence the amount of flux passing through them is practically negligible compared with the flux entering or exiting the barrier through borders AB and GH. Comparisons of analytical results with FEA simulations (Section V) will confirm the soundness of the simplifying hypothesis being assumed.

Once boundary conditions are fixed in the w plane, they automatically transfer to the z plane too; so the rectangle in the z plane will have Neumann boundary conditions applied to sides $A'G'$ and $B'H'$ and Dirichlet boundary conditions applied to sides $A'B'$ and $G'H'$. This leads to conclude that the field solution inside the rectangle domain is given by a

uniform flux density of constant magnitude B_0 oriented along the x-axis (Fig. 5), i.e., in vector form

$$\mathbf{B}'(x, y) = (B_x(x, y)\, B_y(x, y))^t = (B_0\, 0)^t. \tag{26}$$

The vector potential $U'(x, y)$ in the rectangle domain (U' is treated as a scalar quantity coincident with its component along machine axis, which is the only nonzero component) can be obtained from the known relationship [26]

$$B_x(x, y) = -\partial U'(x, y)/\partial y \tag{27}$$

which, applied to (26), yields

$$U'(x, y) = -\int B_x(x, y)dy = -\int B_0 dy = -B_0 y + U_0' \tag{28}$$

where U_0' is an arbitrary additive constant that can be set equal to zero with no loss of generality.

According to conformal map theory [24], knowing the vector potential solution in the z plane automatically leads to know the vector potential $U(u, v)$ in the w plane as follows:

$$U(u, v) = U'(x(u, v), y(u, v)) \tag{29}$$

where functions $x(u, v)$ and $y(u, v)$ are given by (13) and (14). If applied to (28) where $U_0' = 0$, (29) gives

$$U(u, v) = -\frac{B_0}{4}\ln\left[\frac{(\tau/2 + v)^2 + u^2}{(\tau/2 - v)^2 + u^2}\right]. \tag{30}$$

By derivation of the vector potential, the flux density components inside the flux barrier result as

$$\begin{aligned}\mathbf{B}(u, v) &= \begin{pmatrix} B_u(u, v) \\ B_v(u, v)\end{pmatrix} = \begin{pmatrix} -\partial U(u, v)/\partial v \\ \partial U(u, v)/\partial u\end{pmatrix} \\ &= \frac{B_0\tau/2}{((\tau/2 + v)^2 + u^2)((\tau/2 - v)^2 + u^2)} \\ &\quad \begin{pmatrix} u^2 - v^2 + (\tau/2)^2 \\ 2uv\end{pmatrix}.\end{aligned} \tag{31}$$

It is remarked that B_0 represents an unknown constant which, however, does not need to be determined for the purpose of reluctance computation as discussed below.

B. Magnetic Reluctance Computation

The flux barrier magnetic reluctance can be defined as

$$R_b = F_{ED}/\phi_{AG} \tag{32}$$

where F_{ED} is the MMF drop across the barrier [e.g., between points E and D (Fig. 5)], and ϕ_{AG} is the flux passing through the barrier, i.e., (having imposed Dirichlet boundary conditions on segments AB and GH) the flux passing across arc AG. Since the flux density and vector potential field inside the flux barrier are known from (30) and (31), ϕ_{AG} and F_{ED} can be easily computed as follows. Regarding ϕ_{AG} we have

$$\begin{aligned}\phi_{AG} &= L[U(u_G, v_G) - U(u_A, v_A)] = -2L\, U(u_A, v_A) \\ &= \frac{\mathrm{LB}_0}{2}\ln\left[\frac{(\tau/2 + v_A)^2 + u_A^2}{(\tau/2 - v_A)^2 + u_A^2}\right]\end{aligned} \tag{33}$$

where L is the core length. The simplification used in (33) is possible because $u_G = u_A$, $v_G = -v_A$ (Fig. 5) and, therefore, $U(u_G, u_G) = -U(u_A, v_A)$ according to (30).

Regarding F_{ED}, this is computed as (Fig. 5)

$$F_{ED} = \left(\frac{1}{\mu_0}\right)\int_d^{d+h} B_u(u, 0)du. \tag{34}$$

Using (31) in (34) and solving the integral symbolically, we find

$$F_{ED} = (B_0/\mu_0)[\arctan(2(d + h)/\tau) - \arctan(2d/\tau)]. \tag{35}$$

Finally, using (33) and (35) in (32), we can provide an explicit expression for the reluctance R_b as follows:

$$R_b = \frac{2}{L\mu_0}\frac{\arctan(2(d + h)/\tau) - \arctan(2d/\tau)}{\ln\left[\frac{(\tau/2 + v_A)^2 + u_A^2}{(\tau/2 - v_A)^2 + u_A^2}\right]}. \tag{36}$$

Equation (36) shows that the reluctance of a flux barrier only depends on its geometry (parameters d, h, τ, v_A, and u_A shown in Fig. 5) and on machine core length L, while it does not depend on the operating point. Parameter B_0 (which can actually vary from one operating point to the other) appears in both (33) and (35) but cancels out when dividing the two expressions as per (32). The invariance of flux barrier reluctance with respect to the SynRel motor operating point will be proved in Section V [Fig. 15(a)] based on FEA simulations.

C. Energy Stored in a Flux Barrier

For the following, it is worth deriving an analytical expression for the magnetic energy W_b stored in the flux barrier, too. For this purpose, we can observe that magnetic energy is invariant through conformal mappings [24]. Therefore, W_b can be computed as the magnetic energy stored in the rectangle representing the barrier image in the z plane through map $z = f(w)$ (Fig. 5). This is simply

$$W_b = \frac{L\, X\, Y}{2\mu_0}B_0^2. \tag{37}$$

In (37), we can substitute expressions (21)–(23) and (24) and (25) for X and Y and use the expression derived from (33) for B_0: as a result, the following alternative formulation for the energy stored in the barrier is immediately proven:

$$W_b = \left(\frac{1}{2}\right)R_b\, \phi_{AG}^2. \tag{38}$$

V. Application Example and FEA Assessment

In this section, the method presented for computing the reluctance and the stored energy for a circular flux barrier will be illustrated and assessed by applying it to the analytical study of a three-phase SynRel motor whose cross section is shown in Fig. 7. The overall significant design information for the motor are provided in Table I, while the data characterizing flux barrier geometry are provided in Table II. Finally, magnetic saturation is incorporated in the machine stator and rotor cores for the purposes of FEA simulations according to the B–H curved shown in Fig. 8.

Any operating point for the SynRel motor will be univocally defined by specifying the amplitude of the peak stator current I_0 and the electrical angle θ_r between phase a symmetry

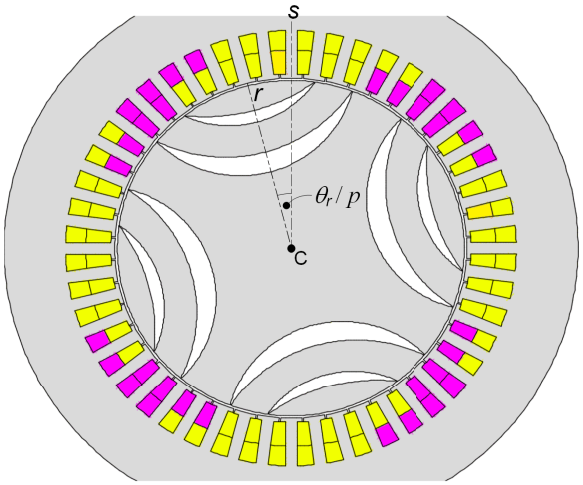

Fig. 7. Sample SynRel motor cross section. Darker coil sides belong to phase a, whose symmetry axis is indicated by s.

TABLE I
CHARACTERISTIC DATA OF THE EXAMPLE THREE-PHASE SYNREL MOTOR

Outer stator radius	350 mm	Number of pole pairs, p	2
Core length, L	750 mm	Number of turns per coil, N_s	5
Outer rotor radius, R	212 mm	Coil to pole pitch ratio	10/12
Air gap width, g	3 mm	Slots per pole per phase, q	4
Number of stator slots	48	Barriers per pole	2

TABLE II
GEOMETRY OF ROTOR FLUX BARRIERS

Outer flux barrier (barrier #1)	Bridge dimensions δ (Fig. 2)	1 mm
	Bridge dimensions ε (Fig. 2)	1.2 mm
	Span angle α (Fig. 2)	22.67°
	Dimension Δ (Fig. 2)	31.9 mm
	Dimension h (Fig. 2)	15.2 mm
Inner flux barrier (barrier #2)	Bridge dimensions δ (Fig. 2)	1 mm
	Bridge dimensions ε (Fig. 2)	1.2 mm
	Span angle α (Fig. 2)	35.52°
	Dimension Δ (Fig. 2)	86.2 mm
	Dimension h (Fig. 2)	25.7 mm

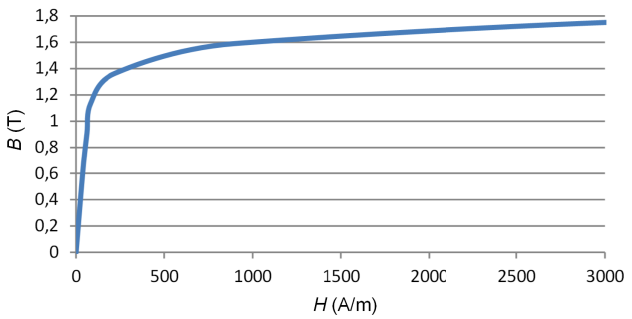

Fig. 8. B–H curve used to characterize the ferromagnetic core.

axis s and the rotor symmetry axis r assumed coincident with barrier axis, as shown in Fig. 7, where p is the number of pole pairs.

The purpose of this paper is to analytically determine the air-gap flux density distribution and the machine torque for a generic operating point and compare results with the same

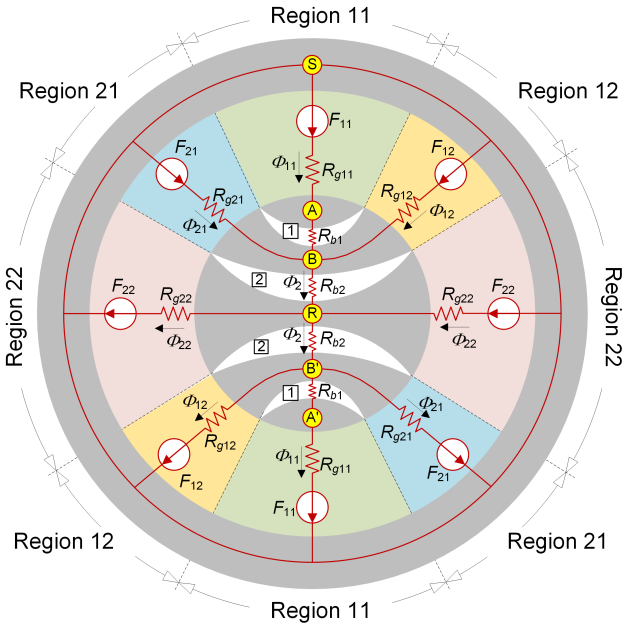

Fig. 9. MEC model schematic for a two-pole SynRel motor with two barriers per pole.

quantities obtained by FEA. For the purpose of analytical simulations, a MEC approach [6], [7], [10], [11] is being adopted, where circular barrier reluctances computed as discussed in Section IV will be used.

A. SynRel Motor MEC Model Definition and Solution

The SynRel motor modeling by MEC method is described referring to the case of a two-pole machine with two barriers per pole, as shown in Fig. 9, where the inner and outer barriers are denoted as 1 and 2. The whole air gap of the machine is subdivided into various regions, marked as 11, 12, 21, and 22, and delimited by the end points of flux barriers, as shown in Fig. 9. Within each air-gap region, a MMF source F_{ij} (with i and j equal to 1 or 2) and an air-gap reluctance R_{ij} are defined as described next, along with the overall flux ϕ_{ij} passing through it. Furthermore, the MEC includes the reluctances R_{b1} and R_{b2} of the two flux barriers, which are, respectively, crossed by fluxes Φ_{11} and Φ_2. Nodes S, A, B, A', B', and R of the MEC denote core regions where no MMF drop is assumed to occur, under the hypothesis of neglecting magnetic saturation except for iron bridges [6], [7], [10], [11]. Finally, as done in [6], [7], [10], and [11], no flux is assumed to flow though iron bridges due to their being small and saturated.

1) Computation of MMF Sources in the MEC: To compute MMF sources F_{ij}, the overall air-gap MMF field due stator currents is first defined. This can be written as [27]

$$F(t,\theta) = \sum_{n=0,1,2} w_n(\theta) \cdot i_n(t) \tag{39}$$

where n is a phase index, ranging from 0 to 2 (0 standing for phase a, 1 for phase b, and 2 for phase c); θ is the angular position (in electrical radians) measured along the mean air-gap circumference and taking the axis s of phase a as the

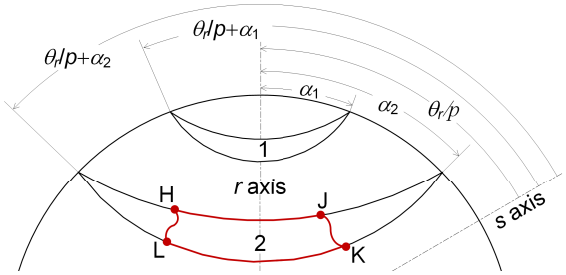

Fig. 10. Mechanical angles for computing MMF sources in the MEC.

zero reference (Fig. 7); $i_n(t)$ is the current in phase n at instant t

$$i_n(t) = I_0 \cos(\omega t - \tfrac{2}{3}\pi n - \varphi_0) \tag{40}$$

$w_n(\theta)$ is the winding function of phase n [27]

$$w_n(\theta) = \sum_{k=1,3,5,..} W_k \cdot \cos\left[k(\theta - \tfrac{2}{3}\pi\ n)\right] \tag{41}$$

$$W_k = \frac{4}{\pi}\frac{N_s}{b}\frac{\sin(\pi\ \cdot k \cdot \gamma\ /2)}{k}\frac{\sin(\alpha_s q k/2)}{\sin(\alpha_s k/2)}. \tag{42}$$

In (40)–(42), φ_0 is an arbitrary initial phase (assumed equal to zero in the following), I_0 is phase peak current, N_s is the number of series-connected turns per coil, b the number of parallel paths per phase, γ the coil to pole pitch ratio, q the number of slots per pole per phase, and $\alpha_s = \pi/(3q)$ the slot pitch angle in electrical radians.

Once the overall air-gap MMF is known from (39)–(42), the MMF sources acting inside the various air-gap regions identified in Fig. 9 are computed as follows:

$$F_{11}(t,\theta_r) = \frac{1}{2\alpha_1 p}\int_{\theta_r-\alpha_1 p}^{\theta_r+\alpha_1 p} F(t,\theta)d\theta \tag{43}$$

$$F_{12}(t,\theta_r) = \frac{1}{(\alpha_2-\alpha_1)p}\int_{\theta_r+\alpha_1 p}^{\theta_r+\alpha_2 p} F(t,\theta)d\theta \tag{44}$$

$$F_{21}(t,\theta_r) = \frac{1}{(\alpha_2-\alpha_1)p}\int_{\theta_r-\alpha_2 p}^{\theta_r-\alpha_1 p} F(t,\theta)d\theta \tag{45}$$

where α_1 and α_2 are the mechanical angles (generically indicated as α in Fig. 2) that characterize the two barriers. From a physical point of view, (43)–(45) represent the mean MMF value inside the various air-gap regions shown in Fig. 9, as further shown in Fig. 10 in terms of mechanical angles.

2) Computation of Air-Gap Reluctances in the MEC: The air-gap reluctances that appear in the MEC can be straightforwardly computed as follows:

$$R_{g11} = (1/\mu_0)g/(2\alpha_1 \mathrm{RL}) \tag{46}$$

$$R_{g12} = R_{g21} = (1/\mu_0)g/[(\alpha_2-\alpha_1)\mathrm{RL}] \tag{47}$$

$$R_{g22} = (1/\mu_0)g/[(\pi/p-\alpha_2)\mathrm{RL}]. \tag{48}$$

3) Computation of Flux Barrier Reluctances in the MEC: The reluctance of rotor circular flux barrier is computed with the procedure discussed in Section IV and, in particular, by means of (36) applied to each of the two barriers per pole.

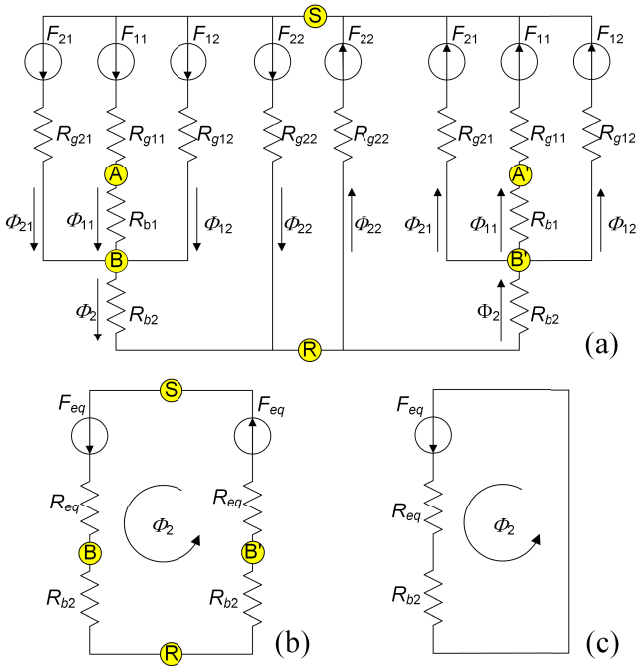

Fig. 11. (a) Overall MEC for a SynRel motor with two barriers per pole. (b) and (c) Simplified equivalent circuits used for MEC solution.

4) MEC Solution: Once all the MEC elements are computed, it can be solved using the well-known methods of circuit theory [28]. The overall MEC for two barriers per pole, resulting from the schematic shown in Fig. 9, is shown in Fig. 11(a). Such circuit can be reduced to the equivalent form shown in Fig. 11(b) and (c), where

$$F_{\mathrm{eq}}(t,\theta_r) = \left[\frac{F_{11}(t,\theta_r)}{R_{g11}+R_{b1}} + \frac{F_{12}(t,\theta_r)}{R_{g12}} + \frac{F_{21}(t,\theta_r)}{R_{g21}}\right] R_{\mathrm{eq}} \tag{49}$$

$$R_{\mathrm{eq}} = \left[(R_{g11}+R_{b1})^{-1} + R_{g12}^{-1} + R_{g21}^{-1}\right]^{-1}. \tag{50}$$

In particular, the fluxes Φ_{11} and Φ_2 are obtained as

$$\Phi_2(t,\theta_r) = F_{\mathrm{eq}}(t,\theta_r)/(R_{\mathrm{eq}}+R_{b2}) \tag{51}$$

$$\Phi_{11}(t,\theta_r) = \frac{F_{11}(t,\theta_r) - \left[F_{\mathrm{eq}}(t,\theta_r) - R_{\mathrm{eq}}\Phi_2(t,\theta_r)\right]}{R_{g11}+R_{b1}}. \tag{52}$$

Once these two fluxes are known, the MMF drops through the two barriers can be computed as

$$\Delta F_1(t,\theta_r) = \Phi_{11}(t,\theta_r)R_{b1}, \quad \Delta F_2(t,\theta_r) = \Phi_2(t,\theta_r)R_{b2}. \tag{53}$$

For the following, it is worth observing that the MMF drops given above apply to whatever path crossing the barrier from one border to the other. Taking the closed path $HJKL$ shown in Fig. 10, for example, Ampere's circuital law assures that the line integral of the flux density field along it is zero (no linked current)

$$\oint_{HJKL} \mathbf{H}\cdot\mathbf{ds} = \int_{HJ}\mathbf{H}\cdot\mathbf{ds} + \int_{JK}\mathbf{H}\cdot\mathbf{ds} + \int_{KL}\mathbf{H}\cdot\mathbf{ds} + \int_{LH}\mathbf{H}\cdot\mathbf{ds} = 0. \tag{54}$$

However, the integrals along arcs HJ and KL are zero due to Neumann boundary condition on them; hence, (54) assures

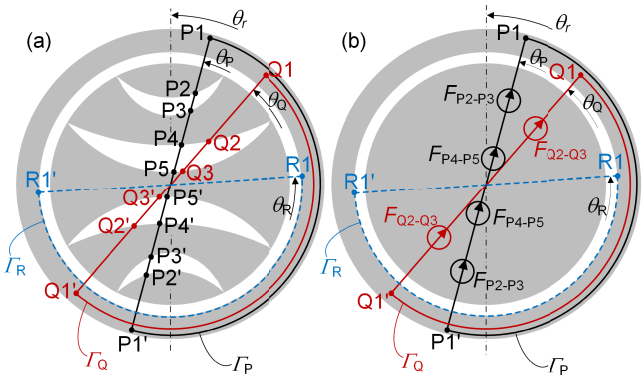

Fig. 12. Closed paths Γ_P, Γ_Q, and Γ_R for computing air-gap field from MEC solution. (a) With actual flux barriers. (b) With equivalent isotropic rotor.

that the MMF drop along path HL is the same as that along path JK. Given the arbitrary choice of points H, J, K, and L, it is concluded that the MMF across the barrier is independent of the path along which it is computed.

B. Air-Gap Flux Density Computation from MEC Solution

Computation of the air-gap flux density from the MEC solution is herein performed by replacing the real SynRel machine rotor [Fig. 12(a)] with an isotropic one [Fig. 12(b)], where the MMF drops occurring across flux barriers are represented by equivalent MMF generators. For example, let us suppose we want to compute the flux density at an instant t (when the rotor is at θ_r) in a point placed at the angular position θ_P [Fig. 12(a)] included in region 11 of the air gap (Fig. 9), i.e., such that $\theta_r - \alpha_1 p \le \theta_P \le \theta_r + \alpha_1 p$; for this purpose, we introduce the closed path Γ_P that crosses the air gap at positions θ_P and $\theta_P + \pi$. The MMF acting on the path, due to stator current, is given by $2F(t,\theta_P)$ according to (39). The MMF drops along Γ_P occur across air gaps and across flux barriers. In particular, the MMF occurring across the outer barriers [i.e., along segments $P2 - P3$ and $P2' - P3'$ in Fig. 12(a)] and across the inner barriers [i.e., along segments $P4 - P5$ and $P4' - P5'$ in Fig. 12(a)] are, respectively, indicated as F_{P2-P3} and F_{P4-P5}. It is therefore clear that, for the purpose of air-gap flux density determination, the SynRel model shown in Fig. 12(a) is perfectly equivalent to the one shown in Fig. 12(b), characterized by the same stator MMF, an isotropic round rotor and MMF sources F_{P2-P3} and F_{P4-P5} instead of the flux barriers. On the other side, based on the considerations made in Section V-A4 (MMF drop invariance with the path), F_{P2-P3} and F_{P4-P5} can be computed through (53) as

$$F_{P2-P3} = \Delta F_1(t,\theta_r), \quad F_{P4-P5} = \Delta F_2(t,\theta_r). \tag{55}$$

As a result, the air-gap flux density at position θ_P with rotor at θ_r will result from Fig. 12(b) and (55)

$$B_g(t,\theta_P,\theta_r) = (\mu_0/g)[F(t,\theta_P) - \Delta F_1(t,\theta_r) - \Delta F_2(t,\theta_r)]. \tag{56}$$

If we are interested in computing the air-gap flux density at a position θ_Q included in the 12 gap region (Fig. 9), i.e., such that $\theta_r - \alpha_2 p \le \theta_Q \le \theta_r - \alpha_1 p$, the closed loop Γ_Q can be introduced, as shown in Fig. 12(a). Unlike Γ_Q, such loop crosses only one (the inner) flux barrier, which results in the equivalent MMF sources indicated as F_{Q2-Q3} in the isotropic-rotor model shown in Fig. 12(b). Based on what has been discussed in Section V-A4, we shall have that $F_{Q2-Q3} = \Delta F_2(t,\theta_r)$, so the flux density at point θ_Q will be

$$B_g(t,\theta_Q,\theta_r) = (\mu_0/g)[F(t,\theta_Q) - \Delta F_2(t,\theta_r)]. \tag{57}$$

Finally, taking a point at position θ_R, placed in the gap region 22 (Fig. 9) the closed loop Γ_R [Fig. 12(a)] can be introduced, which does not cross any rotor barrier. Hence, the air-gap flux density at such position is due to stator MMF only and no rotor MMF drop is to be considered

$$B_g(t,\theta_R,\theta_r) = (\mu_0/g)F(t,\theta_R). \tag{58}$$

The described procedure for air-gap flux density determination is expressed in general terms by means of (59), shown at the bottom of the next page.

To assess the proposed methodology for air-gap field determination, it is applied to the SynRel motor shown in Fig. 7 and characterized by the data given in Tables I and II. The stator winding is energized with a stator currents (40) having a peak value of $I_0 = 50$ A, assigned to the phases according to (40) so that, at $t = 0$, phase a carries the maximum current. FEA simulations of the SynRel motors are then run at $t = 0$, with the given stator current distribution, changing the rotor positions θ_r (measured with respect to the symmetry axis of phase a) and, for each simulation, the normal component of the flux density along the mean air-gap circumference is obtained by FEA, where core saturation effects are included according to the B–H curve given in Fig. 8. FEA simulation results are compared with analytical predictions obtained through the methodology discussed in the previous sections. Comparisons are shown in Fig. 13 for the example rotor positions $\theta_r = 0$, $\theta_r = \pi/6$, and $\theta_r = \pi/3$ electrical radians, showing a satisfactory agreement between numerical and analytical simulation results.

Incidentally, Fig. 13 shows that a peak value of around 0.7 T is reached in the air-gap flux for the operating condition under study. It is noted, however, that the peak flux density in stator teeth exceeds 1.4 T resulting in some local saturation of the stator core and in a quite realistic magnetic loading of the machine. Furthermore, it is noted that the main reason for using a nonlinear B–H curve (Fig. 8) is to produce a natural saturation of rotor iron bridges.

A further check is made reproducing SynRel motor normal operation with the rotor and stator field revolving synchronously at a given electrical speed $\omega = 2\pi/T = 2\pi f$ where $f = 50$ Hz and $T = 20$ ms are the frequency and period of stator currents. Currents are again assigned to phases according to (40) with $I_0 = 50$ A. The initial rotor position ($t = 0$) is set equal to $\pi/4$, so as to reproduce an operating point near the maximum torque capability of the machine (Section V-C). The rotor position is then changed over time as $\theta_r = \omega t + \pi/4$. FEA simulations are run for different instants and the resulting radial air-gap density compared with that obtained analytically from (59) as $B_g(t,\theta,\omega t + \pi/4)$. Comparisons are given in

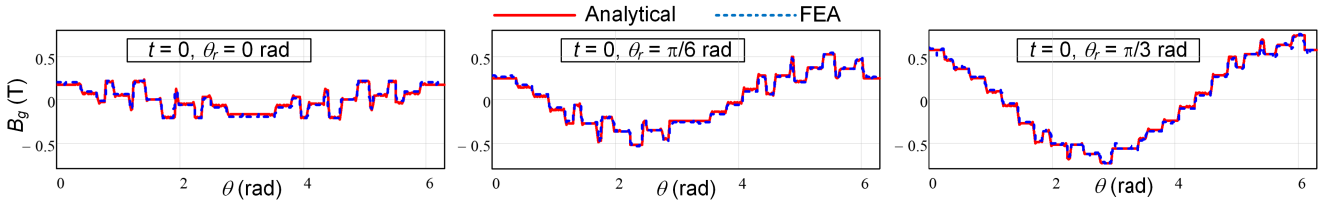

Fig. 13. Flux densities computed analytically and by FEA for $t = 0$ and different rotor angles θ_r. Analytical results are the diagrams of function $B_g(0, \theta, \theta_r)$.

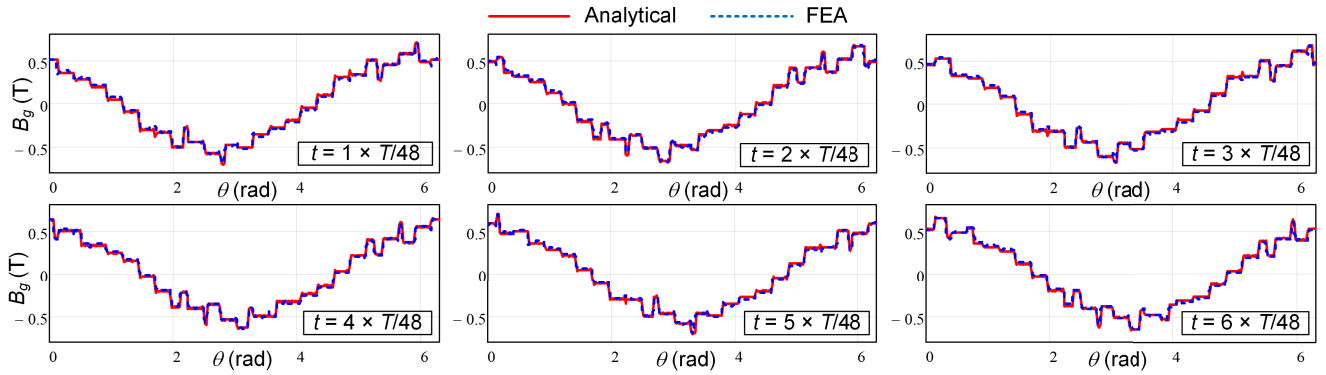

Fig. 14. Flux densities computed analytically and by FEA at different time instants t with rotor moving in synchronism with stator field at speed ω. The rotor position for $t = 0$ is $\theta_r = \pi/4$. Hence, analytical results are the diagrams of function $B_g(t, \theta, \omega t + \pi/4)$ for different instants t.

Fig. 14 for various instants of time and confirm the satisfactory accuracy of the proposed analytical methodology also when applied in the time domain.

Further checks are made using FEA simulations to assess the estimation of flux barrier reluctance and stored energy through (36) and (38), respectively. While the stator currents are kept constant with phase a carrying $I_0 = 50$ A with the other two phases carrying -25 A, the rotor is set at different positions θ_r. For each rotor position, the reluctance of both flux barriers is computed through FEA dividing the MMF drop along the barrier by the flux with flows across it. In addition, the magnetic energy stored in each barrier is computed by FEA. Numerical results are compared with analytical values in Fig. 15 showing a good matching.

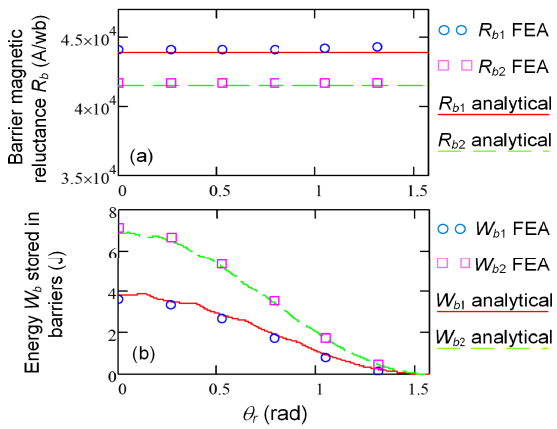

Fig. 15. Comparison between analytical and FEA results for (a) barrier reluctance and (b) energy stored in barriers. Values are plotted as functions of the rotor position θ_r while stator currents are maintained the same.

C. Torque Computation from MEC Solution

The computation of the electromagnetic torque T_{em} from the MEC solution, under the hypothesis of neglecting magnetic saturation, can be performed based on the following relationship:

$$T_{\text{em}}(t, \theta_r) = -\partial W_m(t, \theta_r)/\partial \theta_r \tag{60}$$

where W_m is the total magnetic energy stored in the machine. The magnetic energy W_m is

$$W_m(t, \theta_r) = W_m^{(g)}(t, \theta_r) + W_m^{(b)}(t, \theta_r) \tag{61}$$

$$B_g(t, \theta, \theta_r) = \frac{\mu_0}{g} \begin{cases} F(t,\theta) - \Delta F_1(t,\theta_r) - \Delta F_2(t,\theta_r) & \text{if } (0 \le |\text{mod}(\theta - \theta_r, 2\cdot\pi)| \le \alpha_1/p) \vee (2\cdot\pi - \alpha_1/p \le |\text{mod}(\theta - \theta_r, 2\cdot\pi)| \le 2\cdot\pi) \\ F(t,\theta) + \Delta F_1(t,\theta_r) + \Delta F_2(t,\theta_r) & \text{if } (\pi - \alpha_1/p \le |\text{mod}(\theta - \theta_r, 2\cdot\pi)| \le \pi + \alpha_1/p) \\ F(t,\theta) - \Delta F_2(t,\theta_r) & \text{if } (\alpha_1/p \le |\text{mod}(\theta - \theta_r, 2\cdot\pi)| \le \alpha_2/p) \vee (2\cdot\pi - \alpha_2/p \le |\text{mod}(\theta - \theta_r, 2\cdot\pi)| \le 2\cdot\pi - \alpha_1/p) \\ F(t,x) + \Delta F_2(t,\theta_r) & \text{if } (\alpha_1/p + \pi \le |\text{mod}(\theta - \theta_r, 2\cdot\pi)| \le \alpha_2/p + \pi) \vee (\pi - \alpha_2/p \le |\text{mod}(\theta - \theta_r, 2\cdot\pi)| \le \pi - \alpha_1/p) \\ F(t,x) & \text{otherwise.} \end{cases} \tag{59}$$

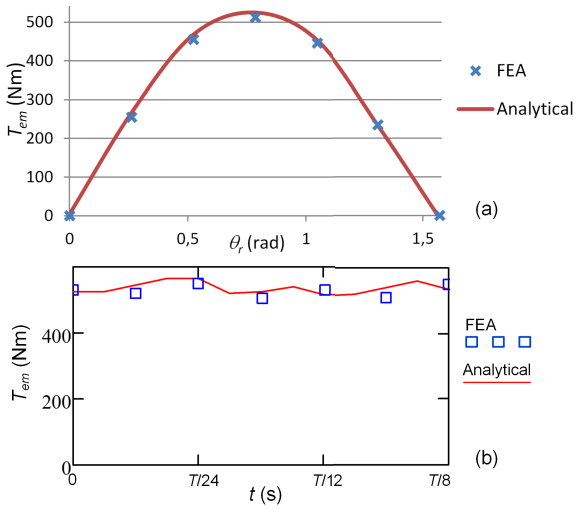

Fig. 16. Comparison between analytical and FEA results for the electromagnetic torque (a) as a function of the rotor position θ_r with fixed stator currents and (b) as a function of time during synchronous operation.

where $W_m^{(g)}$ is the energy stored in the gap and $W_m^{(b)}$ the energy stored in the barriers (no energy is stored in the cores under the hypothesis of their infinite permeability). $W_m^{(g)}$ is approximated as [29], [30]

$$W_m^{(g)}(t,\theta_r) = \frac{\mathrm{L}R_m g}{2\mu_0}\int_0^{2\pi} B_g(t,\theta,\theta_r)^2 d\theta \qquad (62)$$

where $R_m = R + g/2$ is the mean air-gap radius and B_g is the gap flux density given by (59). The energy stored in the barriers, based on Section IV-C and, particularly, based on (38), is

$$W_m^{(b)}(t,\theta_r) = p[R_{b1}\,\Phi_{11}(t,\theta_r)^2 + R_{b2}\,\Phi_2(t,\theta_r)^2] \qquad (63)$$

where Φ_{11} and Φ_2 are the fluxes crossing the two barriers according to (51) and (52). It would not be difficult to substitute the expressions for B_g, Φ_{11}, and Φ_2 into (62) and (63) and perform the integral in (62) symbolically, so obtaining an explicit expression of W_m suitable for analytical differentiation in (60). However, this would imply a considerable burden of symbolical expansions, which are herein omitted due to length limitations. It has been found that acceptable computational performance and accuracy can be easily obtained even if the derivative in (60) is approximated by the difference quotient

$$T_{\mathrm{em}}(t,\theta_r) = -\Delta W_m(t,\theta_r + \Delta\theta_r)/\Delta\theta_r \qquad (64)$$

where $\Delta\theta_r$ is a finite, sufficiently small, increment of θ_r.

Torque values computed with the mentioned method are assessed against FEA simulations. As a first study case, the stator current is kept fixed (with a peak value of $I_0 = 50$ A in phase a and a current of -25 A in the other two cases) and the rotor set at different angles θ_r with respect to phase a symmetry axis. For each rotor position, the torque is computed by FEA and through (64) where $t = 0$ and $\Delta\theta_r = 2\pi/100 = 0.0063$ rad. Results are shown in Fig. 16(a), which highlight an acceptable matching.

Further investigations are conducted by reproducing machine synchronous operation at a working point where the torque takes approximately its maximum value, i.e., with a fixed angle of $\pi/4$ [Fig. 16(a)] between stator MMF axis and the rotor d axis. Stator currents are then set according to (40) with $I_0 = 50$ A and $\omega = 2\pi/T = 2\pi f$ ($f = 50$ Hz, $T = 20$ ms). The rotor position is changed over time as $\theta_r = \omega t + \pi/4$. Torque values are computed through FEA at various instants with a time step $\Delta t = T/48$. Analytical and FEA results are compared in Fig. 16(b). The figure highlights that, although the average torque is quite well met, the torque ripple resulting from the proposed analytical technique is not in very good accordance with that obtained by FEA simulations. The reason for such discrepancy can be easily found in the evident approximation underlying expression (62), where the air-gap energy is estimated neglecting both the tangential flux density component and the flux density variation in the radial direction across the gap. Moreover, the energy derivative in (60) is approximated by the differential quotient in (64).

VI. Conclusion

In this paper, SynRel motors with circular flux barriers have been investigated. A method has been set forth to analytically compute the magnetic reluctance of each rotor barrier (as well as the magnetic energy stored in it) by means of a conformal mapping technique. This result has been used for solving the SynRel motor MEC model for a generic operating point with analytical formulas. From the MEC model solution, the air-gap flux density distribution and the electromagnetic torque estimation have been obtained. Accuracy of results has been assessed by comparison against FEA simulations performed on a sample SynRel motor including magnetic saturation. As a result of FEA-based assessment, the proposed analytical methodology has been proved to be very precise in predicting the air-gap flux density field as well as the reluctance and stored energy of rotor flux barriers. Good accuracy levels have been also found in the estimation of the average torque in a given synchronous operating point. Conversely, further investigations and efforts are required to accurately estimate the torque ripple waveform as well.

VII. Appendix

In this Appendix, the geometric considerations used to derive (4) are explained. The s coordinate s_{C_1} of the point C_1 (Fig. 2) is determined considering that C_1 must have equal distance from both points B and D. Therefore, the quantities

$$\begin{aligned} \overline{DC_1}^2 &= (-R + \Delta + h - s_{C_1})^2 \\ \overline{BC_1}^2 &= (s_{C_1} - s_B)^2 + t_B^2 \end{aligned} \qquad (A1)$$

must be equal. From their equation, s_{C_1} in the form given in (4) is obtained. Similarly, the coordinate s_{C_2} of C_2 is determined considering that C_2 must have equal distance from both points A and E. Therefore, the two quantities

$$\begin{aligned} \overline{EC_2}^2 &= (-R + \Delta - s_{C_2})^2 \\ \overline{AC_2}^2 &= (s_{C_2} - s_A)^2 + t_A^2 \end{aligned} \qquad (A2)$$

must be equal. From their equation, s_{C_2} in the form given in (4) is obtained.

REFERENCES

[1] J. K. Kostko, "Polyphase reaction synchronous motors," *J. Amer. Inst. Elect. Eng.*, vol. 42, no. 11, pp. 1162–1168, Nov. 1923.

[2] T. A. Lipo, "Synchronous reluctance machines—A viable alternative for ac drives?" *Electr. Mach. Power Syst.*, vol. 19, no. 6, pp. 659–671, 1991.

[3] T. Matsuo, A. El-Antably, and T. A. Lipo, "A new control strategy for optimum-efficiency operation of a synchronous reluctance motor," *IEEE Trans. Ind. Appl.*, vol. 33, no. 5, pp. 1146–1153, Sep./Oct. 1997.

[4] J. H. Lee, "Optimum design criteria for maximum torque density and minimum torque ripple of SynRM according to the rated wattage using response surface methodology," *IEEE Trans. Magn.*, vol. 45, no. 3, pp. 1578–1581, Mar. 2009.

[5] J. M. Park, S. I. Kim, J. P. Hong, and J. H. Lee, "Rotor design on torque ripple reduction for a synchronous reluctance motor with concentrated winding using response surface methodology," *IEEE Trans. Magn.*, vol. 42, no. 10, pp. 3479–3481, Oct. 2006.

[6] N. Bianchi, S. Bolognani, D. Bon, and M. D. Pré, "Rotor flux-barrier design for torque ripple reduction in synchronous reluctance and PM-assisted synchronous reluctance motors," *IEEE Trans. Ind. Appl.*, vol. 45, no. 3, pp. 921–928, May/Jun. 2009.

[7] N. Bianchi, S. Bolognani, D. Bon, and M. Dai Pre, "Torque harmonic compensation in a synchronous reluctance motor," *IEEE Trans. Energy Convers.*, vol. 23, no. 2, pp. 466–473, Jun. 2008.

[8] M. Sanada, K. Hiramoto, S. Morimoto, and Y. Takeda, "Torque ripple improvement for synchronous reluctance motor using an asymmetric flux barrier arrangement," *IEEE Trans. Ind. Appl.*, vol. 40, no. 4, pp. 1076–1082, Jul./Aug. 2004.

[9] S. Zhao, O. Wallmark, and M. Leksell, "Low-speed sensorless control with reduced copper losses for saturated PMSynRel machines," *IEEE Trans. Energy Convers.*, vol. 28, no. 4, pp. 841–848, Dec. 2013.

[10] M. Barcaro, N. Bianchi, and F. Magnussen, "Rotor flux-barrier geometry design to reduce stator iron losses in synchronous IPM motors under FW operations," *IEEE Trans. Ind. Appl.*, vol. 46, no. 5, pp. 1950–1958, Sep./Oct. 2010.

[11] M. Barcaro and N. Bianchi, "Air-gap flux density distortion and iron losses in anisotropic synchronous motors," *IEEE Trans. Magn.*, vol. 46, no. 1, pp. 121–126, Jan. 2010.

[12] S. Yamamoto, H. Hirahara, J. B. Adawey, T. Ara, and K. Matsuse, "Maximum efficiency drives of synchronous reluctance motors by a novel loss minimization controller with inductance estimator," *IEEE Trans. Ind. Appl.*, vol. 49, no. 6, pp. 2543–2551, Nov./Dec. 2013.

[13] S. Taghavi and P. Pillay, "A sizing methodology of the synchronous reluctance motor for traction applications," *IEEE J. Emerg. Sel. Topics Power Electron.*, vol. 2, no. 2, pp. 329–340, Jun. 2014.

[14] A. A. Arkadan, N. Al-Aawar, and A. A. Hanbali, "Design optimization of SynRM drives for HEV power train applications," in *Proc. IEEE Int. Electr. Mach. Drives Conf. (IEMDC)*, May 2007, pp. 810–814.

[15] H. Nam, S. B. Park, G. H. Kang, J. P. Hong, J. B. Eom, and T. U. Jung, "Design to improve starting performance of line-start synchronous reluctance motor for household appliances," in *Proc. 39th IAS Annu. Meeting IEEE Ind. Appl. Conf.*, Oct. 2004, p. 85.

[16] H. Kiriyama, S. Kawano, Y. Honda, T. Higaki, S. Morimoto, and Y. Takeda, "High performance synchronous reluctance motor with multi-flux barrier for the appliance industry," in *Proc. 33rd IAS Annu. Meeting IEEE Ind. Appl. Conf.*, Oct. 1998, pp. 111–117.

[17] P. Niazi, H. A. Toliyat, D.-H. Cheong, and J.-C. Kim, "A low-cost and efficient permanent-magnet-assisted synchronous reluctance motor drive," *IEEE Trans. Ind. Appl.*, vol. 43, no. 2, pp. 542–550, Mar./Apr. 2007.

[18] Y.-H. Im, S.-I. Hwang, S.-M. Jang, J.-Y. Choi, and J.-H. Choi, "Analysis of torque pulsation considering interior permanent magnet rotor rib shape using response surface methodology," *IEEE Trans. Magn.*, vol. 48, no. 2, pp. 979–982, Feb. 2012.

[19] P. Alotto, M. Barcaro, N. Bianchi, and M. Guarnieri, "Optimization of interior PM motors with Machaon rotor flux barriers," *IEEE Trans. Magn.*, vol. 47, no. 5, pp. 958–961, May 2011.

[20] J. Wang, V. I. Patel, and W. Wang, "Fractional-slot permanent magnet brushless machines with low space harmonic contents," *IEEE Trans. Magn.*, vol. 50, no. 1, Jan. 2014, Art. ID 8200209.

[21] G. Pellegrino, F. Cupertino, and C. Gerada, "Barriers shapes and minimum set of rotor parameters in the automated design of synchronous reluctance machines," in *Proc. IEEE Int. Electr. Mach. Drives Conf. (IEMDC)*, May 2013, pp. 1204–1210.

[22] R.-R. Moghaddam and F. Gyllensten, "Novel high-performance SynRM design method: An easy approach for a complicated rotor topology," *IEEE Trans. Ind. Electron.*, vol. 61, no. 9, pp. 5058–5065, Sep. 2014.

[23] *Synchronous Reluctance Motor-Drive Packages*. [Online]. Available: http://www.abb.com/product/us/9aac171953.aspx, accessed Mar. 6, 2015.

[24] R. Schinzinger and P. A. A. Laura, *Conformal Mapping: Methods and Applications*. New York, NY, USA: Dover, 2012.

[25] S. D. Fisher, *Complex Variables*. New York, NY, USA: Dover, 1999.

[26] J. D. Jackson, *Classical Electrodynamics*. New York, NY, USA: Wiley, 1999.

[27] A. Tessarolo, "Accurate computation of multiphase synchronous machine inductances based on winding function theory," *IEEE Trans. Energy Convers.*, vol. 27, no. 4, pp. 895–904, Dec. 2012.

[28] J. W. Nilsson and S. Riedel, *Electric Circuits*, 9th ed. Englewood Cliffs, NJ, USA: Prentice-Hall, 2011.

[29] D. Wang, X. Wang, and S.-Y. Jung, "Cogging torque minimization and torque ripple suppression in surface-mounted permanent magnet synchronous machines using different magnet widths," *IEEE Trans. Magn.*, vol. 49, no. 5, pp. 2295–2298, May 2013.

[30] L. Zhu, S. Z. Jiang, Z. Q. Zhu, and C. C. Chan, "Analytical methods for minimizing cogging torque in permanent-magnet machines," *IEEE Trans. Magn.*, vol. 45, no. 4, pp. 2023–2031, Apr. 2009.

Alberto Tessarolo (M'06) received the Laurea degree in electrical engineering from the University of Trieste, Trieste, Italy, in 2000, and the Ph.D. degree in electrical engineering from the University of Padua, Padua, Italy, in 2011.

He was a High-Power Motor and Generator Designer with the Department of Research and Development, Nidec ASI S.p.A., Kyoto, Japan, and joined the University of Trieste in 2006, where he currently serves as an Assistant Professor and teaches the course of Electric Machine Design. He leads several research projects in cooperation with electric machine manufacturers and final users. He has authored around 100 international papers. His current research interests include electric machine modeling and analysis and design optimization.

Dr. Tessarolo is a member of various IEEE societies, such as the IEEE Power and Energy Society, the IEEE Industrial Applications Society, the IEEE Industrial Electronics Society, IEEE Magnetics Society, and the IEEE Reliability Society. He currently serves as an Editor of the IEEE TRANSACTIONS ON ENERGY CONVERSION. He is also a Register Professional Engineer in Italy.